

See discussions, stats, and author profiles for this publication at: <https://www.researchgate.net/publication/224832411>

# Insight into Gold Nanoparticle–Hydrogen Interaction: A Way To Tailor Nanoparticle Surface Charge and Self-Assembled Monolayer Chemisorption

ARTICLE *in* THE JOURNAL OF PHYSICAL CHEMISTRY C · AUGUST 2011

Impact Factor: 4.77 · DOI: 10.1021/jp2054525

CITATIONS

9

READS

47

9 AUTHORS, INCLUDING:



**Alessandra Operamolla**

Università degli Studi di Bari Aldo Moro

41 PUBLICATIONS 183 CITATIONS

SEE PROFILE



**Elena Dilonardo**

Politecnico di Bari

22 PUBLICATIONS 76 CITATIONS

SEE PROFILE



**Pio Capezzuto**

Università degli Studi di Bari Aldo Moro

184 PUBLICATIONS 1,832 CITATIONS

SEE PROFILE



**Giovanni Bruno**

Italian National Research Council

315 PUBLICATIONS 3,305 CITATIONS

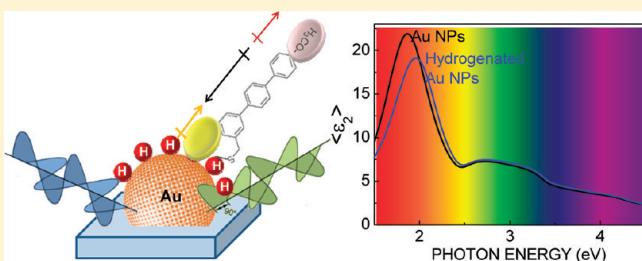
SEE PROFILE

# Insight into Gold Nanoparticle–Hydrogen Interaction: A Way To Tailor Nanoparticle Surface Charge and Self-Assembled Monolayer Chemisorption

Maria M. Giangregorio,\* Maria Losurdo, Giuseppe V. Bianco, Alessandra Operamolla, Elena Dilonardo, Alberto Sacchetti, Pio Capezzuto, Francesco Babudri, and Giovanni Bruno

Department of Chemistry, Institute of Inorganic Methodologies and of Plasmas-CNR-IMIP, via Orabona 4, 70126, Bari, Italy

**ABSTRACT:** The interaction of hydrogen with gold nanoparticles (Au NPs) and gold thin films also functionalized with thiols is investigated. Au NPs deposited on silicon substrates by radio frequency sputtering of a gold target and gold thin films have been exposed to a remote  $H_2$  plasma and subsequently functionalized by the aromatic (4-methoxyterphenyl-3'',5''-dimethanethiol) and aliphatic (dodecanethiol) thiols. The impact of hydrogenation on changes of the charge on gold surfaces and nanoparticles, on the kinetics of the thiol self-assembled monolayer (SAM) formation, and on the density of the resulting SAMs has been investigated combining spectroscopic ellipsometry (SE), Raman spectroscopy, and surface potential Kelvin probe microscopy (SP-KPM) in conjunction with noncontact atomic force microscopy (AFM). We found that remote  $H_2$  plasma pretreatments of gold surfaces are effective in improving thiolate adsorption, making SAMs more uniform and densely packed. We also demonstrate that hydrogenation of nanoparticles improves stability of thiol functionalized Au NPs, avoiding their aggregation. Additionally, we demonstrate that a remote  $H_2$  plasma processing is also effective in the selective removal of the carbon chain and of sulfur atoms from gold surfaces, therefore allowing tailoring of their optical and chemical properties.



## INTRODUCTION

Ultrathin gold films, plasmonic gold nanoparticles (Au NPs), and their functionalization with self-assembled monolayers (SAMs) of organic molecules and biomolecules have attracted interest because of their applications in various fields, including molecular electronics, adhesion promotion, corrosion inhibition, enhancement of the biocompatibility of materials, and modifications of surface properties.<sup>1–3</sup>

Although *n*-alkanethiols on Au(111) are the most thoroughly studied SAMs,<sup>4–7</sup> aromatic thiols have recently received attention due to their (i) high electronic conductivity, (ii) nonlinear optical properties, (iii) molecular rigidity, and (iv)  $\pi$  conjugation.<sup>8</sup> Additionally, polar aromatic thiols with substituent groups can provide SAMs with a dipole moment different from and opposite to common alkanethiols, which can be used to tailor the work function of the metal surfaces on which they are adsorbed<sup>9</sup> and, therefore, to modify the injection barrier between a metal and an organic layer.

From fundamental and technological points of view, there is interest in developing and investigating processes that can modify the properties of the nanosystems and affect their reactivity. Processing of metal surfaces and nanoparticles which can improve the homogeneity of SAMs is searched to produce well-ordered and dense SAMs that can tailor electronic and optical properties in a reliable way. With respect to this, hydrogen processing of Au NPs and films is interesting for all the reasons

listed below. Hydrogen interaction with metal surfaces and nanoparticles as well as with SAMs determines the catalytic and sensing activities of the metal supports as well as the coverage and binding strength of SAMs. Preliminary recent work<sup>10</sup> on the stability and catalytic activity of supported Au NPs has indicated the importance of hydrogen treatment of Au NP based catalysts in stabilizing their catalytic activity.

There is theoretical indication that hydrogen on gold clusters will enhance the charge transfer and may enable gold clusters to be effective for the industrially important catalytic hydrogenation process.<sup>11</sup>

Functionalization and SAM formation also depend on the surface charge of Au thin films and of Au nanoparticles as well. Therefore, processing of gold surfaces and nanoparticles to engineer the surface charge and properly functionalize them is of interest.

As specifically concerns thiol SAMs on gold surfaces, the role of hydrogen on the supporting surface, on the  $-SH$  group binding, and consequently on the chemisorption kinetics of aliphatic and aromatic thiols SAMs is still an open question. Although the process of adsorption of alkanethiols on gold surfaces has been studied extensively, the detailed absorption

Received: June 10, 2011

Revised: August 20, 2011

Published: August 30, 2011

chemistry is still unclear. Generally, the consensus is that the bonding at the interface is via the Au–thiolate (Au–S–R) complex through loss of hydrogen of the S–H groups in the form of  $H_2$ , although the path of formation of molecular hydrogen has not been determined unambiguously.<sup>12,13</sup> In this framework, preadsorbing hydrogen on gold and investigating changes induced into SAM formation may provide further insight into the thiol–gold interaction and provide a way to tailor the SAM anchoring as well.

Finally, from a technological point of view there is a need to develop processes able to selectively remove the organic part functionalizing gold nanoparticles, since the functionalizing/capping agents of nanoparticles may be sometimes detrimental to the sensitivity of gold nanoparticle based field effect transistors (FET).<sup>14</sup>

Gold nanoparticles are catalytically active to hydrogen dissociation, chemisorption, and further reaction more than thin gold films since it has been reported that this activity occurs at surface gold atoms at edges and corners with a lower coordination number.<sup>15,16</sup>

With decreasing the size of Au NPs, the amount of chemisorbed hydrogen on NPs increases, and an increasing fraction is adsorbed strongly, implying that tailoring the hydrogen/gold interface can affect the SAM formation.

Therefore, for all the above-mentioned reasons, investigating the hydrogen–gold and hydrogen–SAM interactions contributes to understanding the surface structure–performance relationship, and to developing processes that can modify the chemistry and charges of interfaces, which ultimately lead to the design of nanostructured systems.

In this paper, the interaction of remote hydrogen plasma with both thin gold films and gold nanoparticles and the impact of this gold–surface hydrogenation on the chemisorption kinetics of aliphatic and aromatic thiol SAMs are investigated. The aim is to develop a nanoparticle/surface processing that can improve the homogeneity of SAMs. We also investigate the interaction of SAMs with hydrogen and the SAM removal kinetics with a twofold purpose: (i) providing insight into the chemistry of the thiol–hydrogen–gold interaction by monitoring in real time the thiol chemisorption kinetics; (ii) developing a processing of SAMs with hydrogen plasmas to achieve either complete thiol ablation from the gold or selective carbon-chain removal, leaving a sulfur passivated/functionalized surface. The peculiarity of the remote hydrogen plasma is that it prevents any heating or sputtering effect and allows a pure chemical SAM ablation by atomic hydrogen without damaging the gold surface and nanoparticles and avoiding the surface contamination by oxidized sulfur species occurring when  $O_2$  or  $N_2$  plasma is used.<sup>17,18</sup>

The study is performed functionalizing both thin gold films and gold nanoparticles (NPs) with the aliphatic *n*-dodecylthiol (C12) and the aromatic 4-methoxyterphenyl-3'',5''-dimethanethiol (TPDMT),<sup>19</sup> which differ in dipole moment as well as in surface packing density and geometry of bonding to gold through one or two sulfur functionalities. The kinetics of the interaction with hydrogen and its impact on SAM optical and structural properties are monitored in real time using spectroscopic ellipsometry (SE), by recording variations of the surface plasmon resonance (SPR) of Au NPs and of the dielectric function of Au thin films. The optical characterization is corroborated by morphological analysis with atomic force microscopy

(AFM) also operating in electric force mode (Kelvin probe) and by structural analysis with Raman spectroscopy.

## ■ EXPERIMENTAL SECTION

**Gold Nanoparticles and SAM Formation and Their Interaction with Hydrogen.** Commercial Au (111) films by Platypus Technologies were used in the present study. They were annealed at 250 °C for 3 h in ultrahigh vacuum (UHV) before dipping in functionalizing solutions.

Au NPs were deposited by radio frequency (13.56 MHz) sputtering an Au target using an Ar plasma under a dc self-bias potential of –500 V. More details about Au NPs can be found in refs 20 and 21.

SAMs were formed by dipping the annealed films in a 1  $\mu$ M ethanol solution of dodecanethiol (C12) or in a 1  $\mu$ M  $CH_2Cl_2$  solution of TPDMT. After dipping, the samples were rinsed with ethanol and  $CH_2Cl_2$ , respectively, and dried with pure nitrogen to remove adsorbed thiol.

The Au films and NPs as well as the C12 and the TPDMT SAMs were exposed to a remote  $H_2$  plasma at room temperature (RT). The remote radio frequency (rf; 13.56 MHz),  $H_2$  plasma operated at a pressure of 1 Torr, a  $H_2$  gas flow rate of 800 sccm, and rf power of 100 W was used as a source of H-atoms. Under those conditions, it was demonstrated<sup>22</sup> that only hydrogen atoms in the ground state interact with the sample and any ion bombardment can be ruled out.

### Atomic Force Microscopy and Kelvin Probe Analysis.

Surface potential Kelvin probe microscopy (SP-KPM) in conjunction with noncontact atomic force microscopy (AFM) were used for the study. Morphology, phase, and surface potential (SP) data were acquired by an AutoProbe CP (ThermoMicroscope) microscope using a gold coated Si tip with a resonant frequency of 80 kHz. Topographical images were used to determine the thin film and NP morphologies and roughness (rms, root-mean-square roughness) while phase images highlighted differing chemisorption of aliphatic and aromatic thiols on gold surfaces also depending on the hydrogen processing. Surface potential (SP) images for SAMs were used to investigate the electrostatic effect of molecular attachment to gold and to provide insight into the structural and electronic properties of the monolayer and its variation depending on the hydrogenation of the Au/SAM interface. The potential is related to the SAM dipole moment (direction, sign, and magnitude) and to the dielectric constant that depend on the structure (chain length, substituents, and conjugation) of the organic adsorbate.<sup>23–29</sup> In order to measure the surface potential, a bias voltage,  $V_{tip} = V_{dc} + V_{ac} \sin \omega t$ , was applied directly to the tip ( $V_{tip}$ ). This results in an electrostatic force,  $F$ , between the tip and the sample given by  $F = (dC/dz)(V_{tip} - V_{sample}) - V_{applied}$ , where  $dC/dz$  is the vertical derivative of the tip–sample capacitance. The SP was determined by adjusting the tip voltage  $V_{tip}$  to nullify the force, so that the tip was at the same potential as the region of the sample surface underneath it. The voltage applied to the tip and the nullifying force were plotted via the in-plane coordinate, thus generating the SP image. The surface potential was referenced with respect to a gold reference sample, whose SP is assumed to be zero, and all these values are relative to this.

Although the absolute values of SP may be affected by air contamination, etc., the qualitative values compare well among different groups, and here, relative variations are considered.

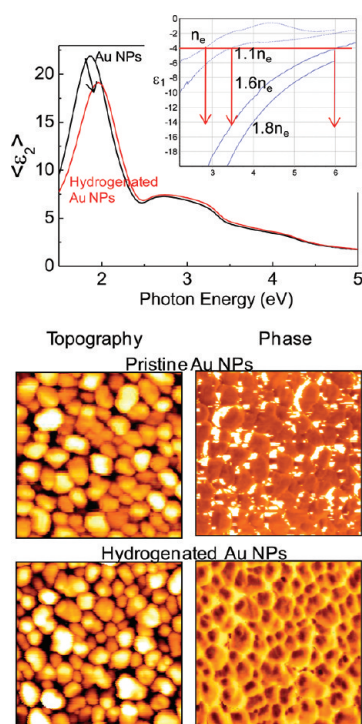


**Figure 1.** Spectra of the imaginary part of the pseudodielectric function,  $\langle \epsilon_2 \rangle$ , of Au NPs before and after exposure to H-atoms. At the bottom, 500 nm  $\times$  500 nm topographic and phase images of Au NPs before and after exposure to H-atoms are shown. The inset shows the blue shift of the plasmon resonance to meet the resonance condition  $\epsilon_1 = -2\epsilon_m$  as defined in the text by increasing the charge density,  $n_e$ , of factors 1.1, 1.6, and 1.8.

**Raman Spectroscopy Analysis.** Surface enhanced Raman scattering (SERS) measurements for the Au NPs/SAM with and without hydrogenation were acquired using a Lab-Ram Jobin Yvon Raman system. The 632.8 nm (1.96 eV) radiation from a He–Ne laser was used as an excitation source. This choice was because it is close to the plasmon resonance wavelength of 729–789 nm (1.57–1.7 eV) of the Au nanoparticles used. The Raman band of a silicon wafer at 520  $\text{cm}^{-1}$  was used to calibrate the spectrometer, and the accuracy of the spectral measurement was estimated to be around 1  $\text{cm}^{-1}$ .

The ordinary Raman spectra of the thiols can be found in ref 19.

**Ellipsometric Analysis.** Ellipsometric spectra of the pseudodielectric function  $\langle \epsilon \rangle = \langle \epsilon_1 \rangle + i\langle \epsilon_2 \rangle = \langle (n + ik)^2 \rangle$ , where  $n$  is the refractive index and  $k$  is the extinction coefficient, were acquired in the energy range 0.75–6.5 eV using a phase modulated spectroscopic ellipsometer (UVISSEL-Horiba Jobin-Yvon) with the possibility of varying the angle of incidence. Measurements were also performed changing the angle of incidence in the range 55–70° and by in-plane rotation to check for any surface anisotropy. However, no variation of the pseudodielectric function was observed by changing both the incidence angle and the in-plane rotation angle. Therefore, data were analyzed in the isotropy approximation. A reason could be the disorder of the SAM formation due to the surface roughness, with respect to the ideal case of ordered SAMs on reconstructed surfaces. Real time kinetic measurements of the pseudodielectric function monitoring the interaction with atomic hydrogen were carried out with a time resolution of 1 s.

Spectroscopic ellipsometry (SE)<sup>30</sup> has been shown to be a valuable technique for SAM characterization of thickness and refractive index.

SE spectra were analyzed using a simple one-layer (three-phase) model (substrate/SAM/air). The dielectric functions of the gold substrate were measured after each processing step and entered as substrates in the modeling.

The optical constants for the C12 and TPDMT were set in a previous work.<sup>19</sup>

Furthermore, SE has also been demonstrated to be suitable in the case of the optical analysis of Au NPs through the monitoring of the surface plasmon resonance (SPR)<sup>21</sup> and of its modification upon the hydrogenation of NPs and the formation of SAMs.

## RESULTS AND DISCUSSION

**H<sub>2</sub> Remote Plasma Treatment of Gold Films and of Plasmonic Gold Nanoparticles.** Figure 1 shows the spectra of the imaginary part of the pseudodielectric function,  $\langle \epsilon_2 \rangle$ , of Au NPs before and after exposure to H-atoms. The Au NP SPR peak at 1.86 eV (666 nm) is very sensitive to surface modification and to charge density variation of the NPs. Specifically, a blue shift to 1.97 eV (629 nm) and damping of the Au NP SPR is observed upon Au NP hydrogenation. This variation is not due to a morphology change of the NPs as confirmed by similar AFM images acquired for the NPs before and after H-atom exposure and also shown in Figure 1. Indeed, this blue shift can be ascribed to an increase of electron density at the NP surface, due to electron transfer from the H-atoms to the Au NPs.

This blue shift can be rationalized by the charge transfer considering that the resonance condition for the plasmon absorption is roughly fulfilled when

$$\epsilon_1 = -2\epsilon_m \quad (1)$$

where  $\epsilon_1$  is the real part of the dielectric function of the metal and  $\epsilon_m$  is the dielectric function of the medium where NPs are embedded, and according to the Drude model  $\epsilon_1$  is related to the plasmon frequency of the metal, which, in turn, depends on the charge density,  $n$ , in the metal NPs according to the following expression:<sup>31</sup>

$$\epsilon_D(\omega) = 1 - \frac{\omega_p^2}{\omega^2 + i\gamma\omega} \quad (2)$$

where

$$\omega_p^2 = \frac{ne^2}{\epsilon_0 m_{\text{eff}}} \quad (3)$$

is the plasmon frequency expressed in terms of the electron density,  $n$ , the electron charge  $e$ , the vacuum permittivity,  $\epsilon_0$ , and the electron effective mass,  $m_{\text{eff}}$ , while  $\gamma$  is the damping constant of the resonance. According to eqs 2 and 3, the position of the plasmon band depends on  $\omega_p$ , which itself varies as the square root of  $n$ , the electron density inside the NP. As a consequence, the plasmon band is displaced upon adding or subtracting electrons to the overall metallic core. Specifically, an increase of the electron density in the NPs causes the  $\epsilon_1$  to become more negative, meeting the resonance condition (1) at a lower wavelength, as shown by the simulation in the inset of Figure 1. Therefore, charge transfer from the hydrogen to the NPs leads to an increase in  $n$ , which induces the observed slight SPR blue shift. This increase in the NP charge density is consistent with the



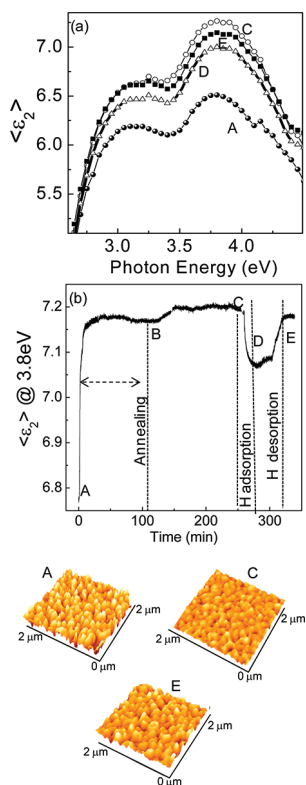
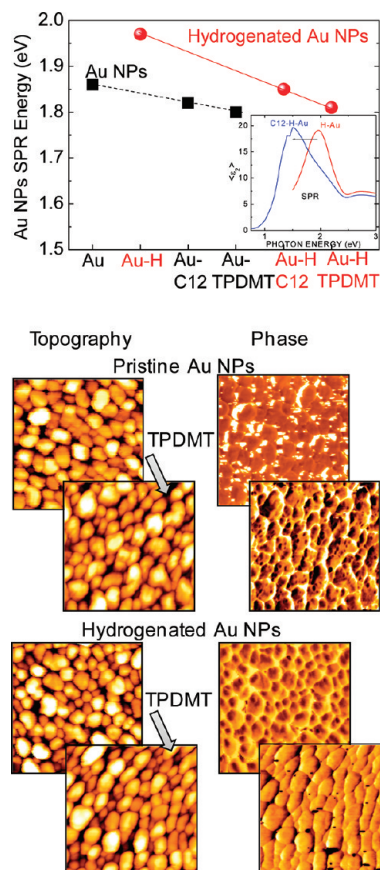


**Figure 2.** (a) Room temperature  $\langle \epsilon_2 \rangle$  experimental SE spectra, in the energy range 2.5–4.5 eV, of the Au(111) substrate as-received (A, solid circles), after annealing (C, open circles), after hydrogen plasma adsorption (D, open triangles), and after hydrogen desorption (E, solid squares). A, C, D, and E spectra refer to points in (b). (b) Real time evolution of the imaginary part,  $\langle \epsilon_2 \rangle$ , of the pseudodielectric function of the gold substrate during annealing at 250 °C in UHV for 3 h and subsequent exposure to remote  $H_2$  plasma. The  $2 \mu\text{m} \times 2 \mu\text{m}$  tridimensional AFM topographical images of the Au(111) substrate as-received (A) (rms = 2 nm), after annealing (C) (rms = 1.5 nm), and after hydrogen desorption (E) (rms = 1.6 nm) are also shown as insets. The vertical scale is 0–17.2 nm.

donor character of H-atoms adsorbing at the low-coordinated sites of the NP surface,<sup>32</sup> and is consistent with previous reports that Au NPs can store charge.<sup>33</sup> Specifically, previous theoretical works demonstrated that Au hydrides at the NP surface, such as  $\text{AuH}_2^-$  and  $\text{AuH}_4^-$ , are stabilized by relativistic effects<sup>34</sup> and their formation is favored in electron-rich systems like laser ablation and plasma processes; therefore, the presence of hydrogen may increase charge transfer to Au NPs (negative charge on the hydrogenated Au NPs).

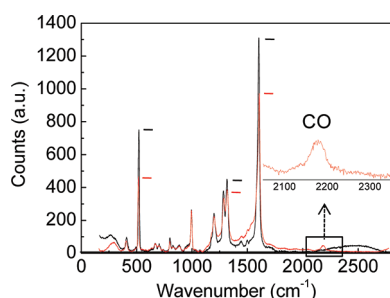
This electron transfer to Au NPs has been corroborated by X-ray photoelectron spectroscopy data of the Au 5d band, which also shows a shift of a few tens of millielectronvolts to lower binding energy, and can be also inferred by the comparison of phase images (see Figure 1) showing a different friction for the hydrogenated NPs and, hence, a different Au phase (while the phase image for the pristine Au NPs shows a homogeneous contrast due to metallic Au for the NPs; the bright regions are simply holes between the NPs).

Figure 2a shows the  $\langle \epsilon_2 \rangle$  SE spectra of the Au(111) film, as received (spectrum A), after annealing (spectrum C), after hydrogen adsorption (spectrum D), and after hydrogen desorption (spectrum E), which correspond to the A-, C-, D-, and E-points in Figure 2b that show the real time evolution of  $\langle \epsilon_2 \rangle$



**Figure 3.** Shift of the SPR peak for NPs with and without hydrogenation functionalized with both TPDMT and C12. The inset shows the shift of the SPR in the spectra of  $\langle \epsilon_2 \rangle$ . At the bottom, 500 nm  $\times$  500 nm topographic and phase images of Au NPs before and after functionalization with TPDMT with and without hydrogenation are shown.

during annealing of the gold film at 250 °C in UHV for 3 h and subsequent exposure to remote  $H_2$  plasma. The initial increase in the  $\langle \epsilon_2 \rangle$  value is indicative of contaminant removal from the surface, as well as of gold grain size increase,<sup>35</sup> as also confirmed by the AFM topographical images in Figure 2. The AFM images also show a decrease of the rms from 2 to 1.5 nm upon annealing. Once contaminants have been removed and grain size reaches equilibrium at this temperature (annealing at higher temperatures must be avoided because of out diffusion of titanium primer),<sup>19</sup> an almost flat  $\langle \epsilon_2 \rangle$  profile is recorded. At the B-point, the sample is cooled to room temperature that is reached at the C-point. As soon as the remote  $H_2$  plasma is turned on (C-point), a decrease of  $\langle \epsilon_2 \rangle$  is observed. However, as soon as the  $H_2$  plasma is turned off (D-point), the  $\langle \epsilon_2 \rangle$  trend reverses, indicating that the interaction of a clean gold surface with H-atoms is a reversible phenomenon due to adsorption/desorption and in-out diffusion processes, without significant roughening of the gold surface, as measured by AFM. Nevertheless, a slight difference is measured in the  $\langle \epsilon_2 \rangle$  spectra before and after hydrogen exposure, which is due to hydrogen adsorption on the gold surface, consistently with previous studies.<sup>36</sup> Although bulk gold is not able to absorb molecular hydrogen, polycrystalline and clustered gold show catalytic activity that leads the dissociation and adsorption of hydrogen limited to the gold atoms at corner and edge positions.<sup>36</sup> Here, we are already in the



**Figure 4.** Raman spectra of Au NPs functionalized by TPDMT with (black line) and without (red line) hydrogenation. The inset highlights the CO adsorption that is absent in the spectrum of the hydrogenated Au NPs. Small marks are only to emphasize the SERS enhancement.

presence of hydrogen atoms generated by the plasma source, which can be incorporated easily into the surface and subsurface of thin Au films. According to Stobirski et al.,<sup>37</sup> some of the chemisorbed hydrogen exists in the form of weakly bonded dimers that can desorb also via the Eley–Rideal mechanism, consistently with the fast increase of the  $\langle \varepsilon_2 \rangle$  observed in Figure 2b when the hydrogen plasma is turned off. Furthermore, Bus et al.<sup>38</sup> found that atomic hydrogen chemisorbed on gold is stable on the surface after evacuation at 373 K for 2 h. This strongly surface chemisorbed hydrogen gives a reason for the incomplete recovering of the  $\langle \varepsilon_2 \rangle$  value after the hydrogen exposure in Figure 2a.

**Thiol Adsorption on Gold Films and on Nanoparticles Modified by Hydrogen.** As for the functionalization of hydrogenated Au NPs, Figure 3 shows the SPR peak shift for NPs with and without hydrogenation functionalized with both TPDMT and C12. A larger red shift is found for SAMs on hydrogenated NPs. It is known that the SPR spectral shift ( $\Delta\lambda$ ) in response to changes in refractive index is approximately given by

$$\Delta\lambda \approx m(n_{\text{SAM}} - n_{\text{medium}})(1 - e^{-2d/l_d}) \quad (4)$$

where  $m$  is the sensitivity factor (in nanometers per refractive index unit) and depends on a specific molecule,  $n_{\text{SAM}}$  and  $n_{\text{medium}}$  are the refractive indices of the forming SAM and of the medium surrounding the nanoparticle, respectively,  $d$  is the effective thickness of the SAM (in nm), and  $l_d$  is the electromagnetic field decay length (in nm).<sup>39</sup> Therefore, a red shift may occur because of the increase in the SAM refractive index, as already demonstrated by previous studies.<sup>40</sup>

Therefore, considering that, keeping the same geometry of NPs, i.e., constant  $m$  and  $l_d$  in eq 4, the shift depends on the refractive index of the capping layer, on coverage, and on charge transfer of the SAM, it may be inferred that hydrogenation of NPs induces a higher coverage by the thiols, and/or a more effective charge transfer from the NPs to thiols. Specifically, previous studies<sup>41,42</sup> have shown that Au NPs transfer conduction band d-electrons from Au-atoms to S-atoms when functionalized with strongly interacting thiols. Therefore, from the larger red shift of the hydrogenated Au NPs in Figure 3, it can be inferred that a more effective charge transfer and stronger Au–S bond form when mediated from hydrogen preadsorbed on the NPs (see discussion below). This stronger interaction of the thiol with the hydrogenated Au NPs results in more homogeneous SAMs, as shown from the phase images at the bottom of Figure 3. Specifically, a nonhomogeneous dark contrast related to non-homogeneous thiol chemisorption on the pristine Au NPs is

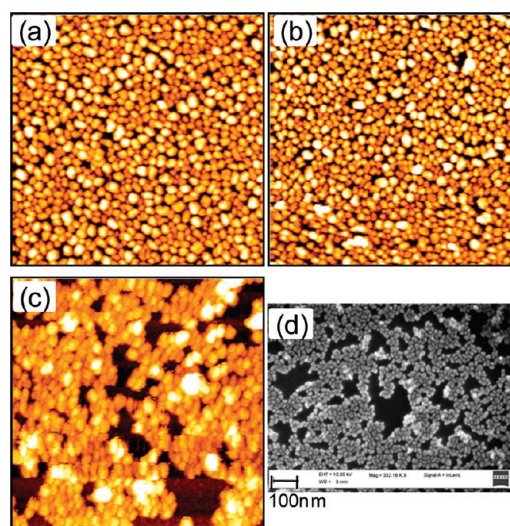


**Figure 5.** The  $2\ \mu\text{m} \times 2\ \mu\text{m}$  topographical images of Au NPs (a) before and (b) after hydrogenation and C12 adsorption and (c) after C12 adsorption without hydrogenation. (d) SEM image of non-hydrogenated Au NPs functionalized with C12.

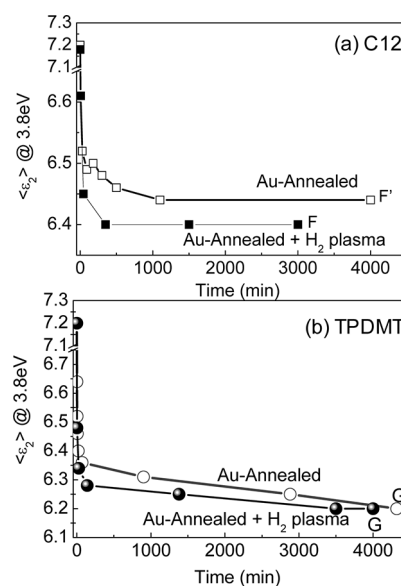


**Figure 6.**  $\langle \varepsilon_2 \rangle$  kinetic profile acquired during (a) C12 and (b) TPDMT adsorption on annealed gold substrates with (solid symbols) and without (open symbols) hydrogen plasma exposure.

seen, while a very homogeneous phase and, hence, homogeneous thiol SAM is promoted on hydrogenated Au NPs. This is also corroborated by an enhancement of the SERS effect as shown in the Raman spectra of the TPDMT in Figure 4, which also indicates that hydrogenation of Au NPs is effective in removing any possible competitive contaminant such as CO adsorption on Au (seen for the SAM on pristine Au NPs but absent in the spectrum of the hydrogenated Au NPs).

Another advantage of the H-atom treatment of the Au NPs is shown in the AFM images of Figure 5. Here, the AFM images of thiol functionalized Au NPs with and without hydrogenation are compared. While the C12 thiol functionalization of pristine Au NPs results in reaggregation of NPs, their hydrogenation imparts



appreciable stability to the nanoparticles during the functionalization, as shown by the AFM.

As for hydrogenation of Au thin films, parts a and b of Figure 6 show the  $\langle \varepsilon_2 \rangle$  kinetic profiles acquired during, respectively, C12 and TPDMT adsorption on annealed gold films with and without hydrogen plasma exposure. The decrease of  $\langle \varepsilon_2 \rangle$  is indicative of the SAM formation, and it can be due to an increase of the SAM thickness and/or an increase of the refractive index of the SAM layer, i.e., surface coverage.

Considering that for C12 a refractive index of 1.45–1.5 is reported in the literature,<sup>43–45</sup> a change in refractive index, due to a change in surface coverage, in the range 1.2–1.45, or a change in thickness in the range 10–16 Å will imply a change in the ellipsometric parameter  $\Psi$  of 0.01°, which is actually comparable to the accuracy of the used ellipsometry, and a change in the ellipsometric parameter  $\Delta$  of 0.04° (the ellipsometer accuracy for  $\Delta$  is also 0.01). This consideration rules out the simultaneous determination with high accuracy of both thickness and refractive index. Therefore, in the following known geometric constraints on thickness are considered in order to interpret data in terms of surface coverage variation.

Indeed, many previous studies on the adsorption of C12 on gold using infrared reflection absorption spectroscopy<sup>46</sup> and X-ray photoelectron spectroscopy<sup>47,48</sup> have established a tilt angle of 30° for C12 chemisorbed on Au(111). Furthermore, a previous study has argued and demonstrated that the value of the tilt angle of thiols on the rough Au surface is probably not different from that on the continuous flat substrate.<sup>49</sup> Additionally, in a previous work on aromatic thiols,<sup>19</sup> density function theory calculations have shown that an upright ring orientation is consistent with the energy minimum configuration for the TPDMT, i.e., a 0° tilt angle. These geometries of binding to gold for the C12 and TPDMT correspond to SAM thicknesses of 16.8 and 18.9 Å.<sup>19</sup> Moreover, a multisample analysis of SAMs at the steady state conditions for the two thiols prepared by us has given thicknesses of  $16.1 \pm 1.2$  and  $18.2 \pm 1.5$  Å, respectively for C12 and TPDMT. Therefore, in the present study, we have assumed and fixed the above tilt angles and, hence, the film thickness. Nevertheless, we cannot rule out a possible rotation of molecules around the long axis, which is actually likely considering the surface roughness of the sample (and curvature of nanoparticles) and considering also previous studies that have reported that an ordered herringbone structure of aliphatic thiols is preserved up to 300 K and that somewhere between 300 and 325 K the chains start to rotate along the long axis, yielding some disorder.<sup>50</sup> Indeed, the formation of nonhomogeneous domains with different rotations around the long axis will reduce the packing density of the thiol molecules, and, therefore, will lead to a lower effective SAM refractive index. Therefore, we have interpreted the observed variation of  $\langle \varepsilon_2 \rangle$  in terms of variation of density, i.e., refractive index of SAM, since it is well-known that the refractive index of a material is a function of its density, leading to the Lorentz–Lorenz formula that can be used to transform the calculated refractive index to a surface coverage.<sup>51,52</sup> Specifically, the comparison of the kinetic profiles with and without preexposure of the gold substrates to the remote H<sub>2</sub> plasma shows that hydrogenation of the annealed gold surface promotes a faster thiol adsorption on gold. The saturation value indicates that the SAM equilibrium has been reached. Therefore, the kinetic profiles as well as spectra indicate a promoted thiol adsorption on hydrogenated gold surfaces, as discussed in the section Interaction of C12 and TPDMT SAMs

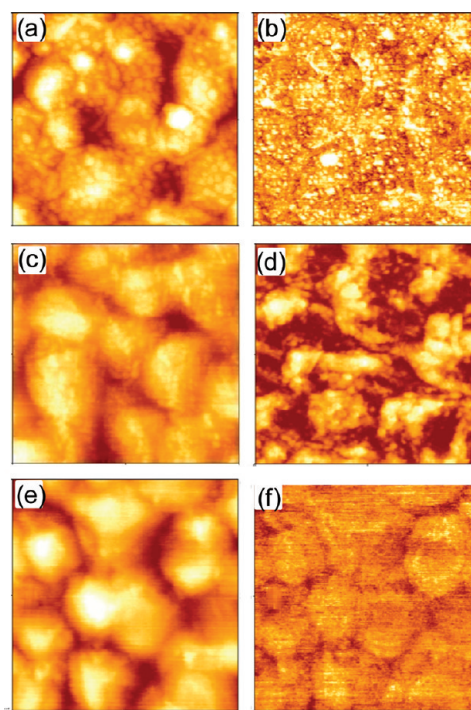
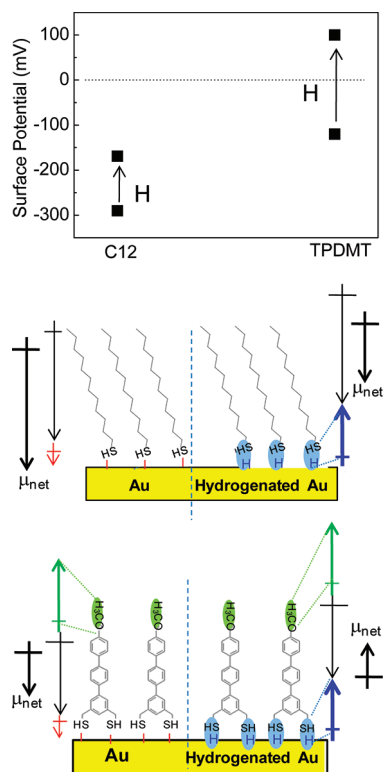


**Figure 7.** (a, b) Respectively,  $2 \mu\text{m} \times 2 \mu\text{m}$  topographical and phase images of C12 SAM on gold with hydrogen plasma gold pretreatment. (c, d) Respectively,  $2 \mu\text{m} \times 2 \mu\text{m}$  topographical and phase images of C12 SAM on gold without hydrogen plasma gold pretreatment. The  $2 \mu\text{m} \times 2 \mu\text{m}$  (e) topographical and (f) phase images of the TPDMT SAM are also shown. The vertical scale is 0–17.2 nm for topographical images and 9.63–10.54 V for phase images.

with Hydrogen. Specifically, Figure 6a shows that the time to reach equilibrium for C12 decreases from 18 to 6 h for hydrogenated gold. Similarly, the adsorption equilibrium is reached after 3 h instead of 15 h for TPDMT.

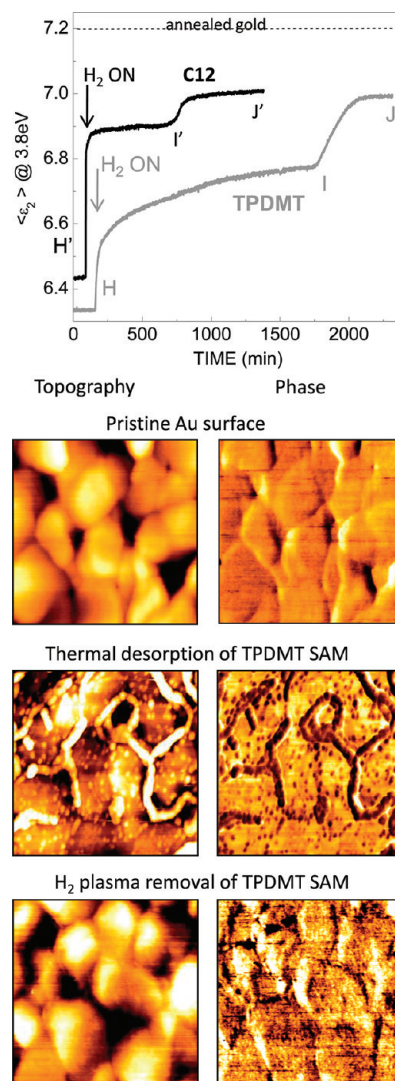
Figure 7 shows the  $2 \mu\text{m} \times 2 \mu\text{m}$  topographical and phase images of the C12 SAM on gold film with and without hydrogenation. Interestingly, similarly to Au NPs, also for Au thin films the phase image shows areas that can be associated with nonuniform distributed C12 SAM agglomerates (lighter spots) on the simply annealed gold surface. Conversely, hydrogenation of the gold film results in a more uniform distribution and higher coverage of the C12 SAM. The TPDMT SAM shows always a very homogeneous coverage/distribution in the phase image.

Figure 8 shows the variation of the surface potential for the C12 and TPDMT SAMs obtained on Au films with and without hydrogen treatment. The C12 SAM on Au shows a negative potential of  $-290 \pm 10$  mV, while for the TPDMT SAM the negative potential is  $-120 \pm 10$  mV, consistent with SP values reported in the literature for thiols<sup>23,53</sup> (the negative sign is because the surface potential is measured with respect to a bare Au reference).<sup>28</sup> The surface potential depends on the dipole moment of the alkyl or aromatic chain part and on the ionic properties of the  $\text{Au}^+ - \text{S}^-$  bond (the bonding of sulfur and gold at the atomic level involves a sharing of electrons from the gold to the sulfur atom, with negative charge on the S atom). However, according to previous works and also theoretical calculations, the contribution of the S–Au bond to the surface potential is negligible with respect to that of the chain,<sup>54</sup> mainly because the  $\text{Au}^+$  charge can be screened by the electrons within the metal,



**Figure 8.** Variation of surface potential for C12 and TPDMT SAMs with and without hydrogen plasma gold pretreatment. At the bottom a simple schematic representation of the various dipoles contributing to the surface potential and their variations are shown for a qualitative explanation of the variation observed. The black arrow represents the C-chain contribution; the red arrow is for the Au–S dipole; the green arrow is for the OCH<sub>3</sub> dipole; the blue arrow represents qualitatively the interface dipole variation due to hydrogenation of the gold surface. The net dipole,  $\mu_{\text{net}}$ , is also shown.

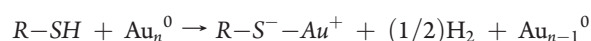
while this may not be the case for the organic SAM. Therefore, variation in the SP as well as its different initial values for the two thiols relates to the different molecular structure, packing, and orientation of the SAM, and/or to the formation of an interface dipole at the SAM/Au interface. For the TPDMT SAM, the surface potential is affected by the –OCH<sub>3</sub> groups on the  $\pi$ -conjugated triphenyl backbone, which contributes with a negative charge due to the electronegativity of the oxygen atoms (see blue arrows in the scheme of Figure 8), yielding a net dipole moment of opposite direction, as sketched at the bottom of Figure 8. Upon hydrogen treatment of the gold surface, for both SAMs the SP increases to  $-155 \pm 5$  mV for C12 SAM, while it changes sign for the TPDMT SAM; the change in SP is larger for TPDMT than for C12. Two reasons can be invoked to explain the observed change: one reason is the presence of an additional interface dipole at the Au–S interface with polarity opposite to the conventional  $\text{Au}^+ - \text{S}^-$ , as sketched in Figure 8. This interface dipole would be consistent with the electron transfer from hydrogen to Au and accumulation of negative charge on Au (see discussion about Figure 1). The second reason may be related to the improved order and packing density of the SAMs upon hydrogenation (consistent with the ellipsometry data, which showed an increase of the refractive index of SAMs upon hydrogenation), since the



**Figure 9.**  $\langle \epsilon_2 \rangle$  time evolution, recorded at 3.8 eV, during exposure of C12 and TPDMT SAMs to H-atoms. The black dotted line represents the  $\langle \epsilon_2 \rangle$  value of the annealed gold substrate. 500 nm  $\times$  500 nm AFM topography and corresponding phase images for gold films before any treatment and after thermal desorption and H<sub>2</sub> plasma removal of TPDMT SAM.

surface potential increases with the increase in density of molecules.<sup>55</sup>

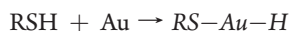
This increase in the order and packing density of the SAMs upon hydrogenation of gold can be rationalized as follows. The formation of the SAM has been considered as an oxidative addition of the S–H bond to the gold surface, followed by a reductive elimination of hydrogen; i.e., the following adsorption chemistry can be schematized:



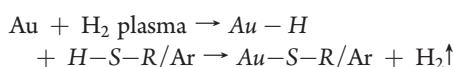
The cleavage of the S–H bond has been identified as the key factor leading to the chemisorption of the thiolate. However, the direct formation of molecular H<sub>2</sub> is a kinetically hindered event that would require the co-reaction of two neighboring thiol molecules or the interaction of a surface H-site with the gas phase (abstraction by Eley–Rideal) or with another chemisorbed H



(Langmuir–Hinshelwood diffusive collision):



Conversely, in the present case of hydrogenated gold, we should consider that, first, atomic hydrogen has been demonstrated to be effective in the removal of organic species from the gold surface, yielding a larger number of active sites for the thiol adsorption. Furthermore, the exposure of gold to a remote  $\text{H}_2$  plasma yields chemisorption of H-atoms on the surface, which aids the thiol S–H cleavage by the surface process where each adsorbed thiol reacts with an H-atom on the surface according to the process



This reaction is consistent with the theoretical prediction indicating that hydrogen cleavage is energetically favored when a path for formation of molecular hydrogen is provided,<sup>38</sup> and with the observed faster chemisorption kinetics and higher thiol coverage.

#### Interaction of C12 and TPDMT SAMs with Hydrogen.

Figure 9 shows the  $\langle \varepsilon_2 \rangle$  time evolution recorded at 3.8 eV during the exposure of the C12 and TPDMT SAMs to H-atoms. The black dotted line represents the  $\langle \varepsilon_2 \rangle$  value of the annealed gold substrate.  $\text{H}'$  and  $\text{H}$  represent the  $\langle \varepsilon_2 \rangle$  values for the C12 and TPDMT SAMs, respectively, which show different behaviors upon exposure to H-atoms. Specifically, for the C12 SAM,  $\langle \varepsilon_2 \rangle$  quickly increases when the remote  $\text{H}_2$  plasma is turned on, until a saturation value is reached. The increase in the  $\langle \varepsilon_2 \rangle$  value to approach the value of the dielectric function characteristic of bare gold (represented by the dashed line in Figure 9) indicates a reduction in thickness and/or coverage of the overlayer on gold and, hence, is consistent with SAM aliphatic chain desorption. However, when we increase the H-atom density interacting with the substrate ( $\text{I}'$ -point), a further  $\langle \varepsilon_2 \rangle$  increase is observed until a new plateau value is reached ( $\text{J}'$ -point) and no further modifications are observed even with prolonged exposure to H-atoms.

Conversely, when the TPDMT SAM is exposed to H-atoms, a slower  $\langle \varepsilon_2 \rangle$  increase is observed until the saturation value ( $\text{I}$ -point) is reached followed by a larger and more rapid variation when the H-atom density is increased (from  $\text{I}$ -point to  $\text{J}$ -point). Those different kinetics can be explained by considering that the sulfur is the most difficult atom to remove from the surface because of its high affinity for gold.<sup>56</sup> Therefore, the two-step  $\langle \varepsilon_2 \rangle$  kinetics can be attributed respectively to the selective desorption of the hydrocarbon (C–H) chain and to sulfur (as  $\text{H}_2\text{S}$ ) later on, as confirmed by the X-ray photoelectron spectroscopy (XPS) analysis in the S 2p region which showed still S bound to Au at the  $\text{I}$ -point and no sulfur at all at the  $\text{J}$ -point. Furthermore, the AFM data at the bottom of Figure 9 emphasize the advantage of the selective removal of the SAM by the H-atom treatment, yielding a gold surface similar to the initial one, whereas the thermal treatment at  $T > 450^\circ\text{C}$  needed to completely remove the sulfur from the surface, completely damaging the Au thin film and causing even interdiffusion of the primer (the dark spots and lines in the phase image) through the grain boundaries. Therefore, the selective ablation of the organic (C–H) and

inorganic (sulfur) parts by H-atoms is interesting from a technological point of view to obtain sulfur-terminated gold for anchoring other molecules.

## CONCLUSIONS

In summary, we have investigated the interaction of atomic hydrogen with gold surfaces and nanoparticles and the effect of chemisorbed hydrogen on the SAM formation of aliphatic (C12) and aromatic (TPDMT) thiols. The kinetics of the surface and nanoparticle modifications during hydrogen exposure and its impact on the kinetics of SAM formation have been monitored in real time exploiting spectroscopic ellipsometry. Modifications of surface charge induced by the hydrogenation have been probed by electrical force microscopy. It is shown that treatment of gold thin films and nanoparticles with atomic hydrogen is a valuable process to do the following:

- Stabilize gold nanoparticles with respect to self-aggregation.
- Form denser and more homogeneous SAMs of aliphatic and aromatic thiols.
- Remove selectively the carbon chain and/or sulfur moieties of functionalizing layers.

A mechanism based on the modification of the charge at the Au/S interface and on the thiolate binding formation is proposed to explain the observed enhancement of thiol chemisorption.

## AUTHOR INFORMATION

### Corresponding Author

\*E-mail: michelaria.giangregorio@ba.imip.cnr.it. Phone: (+39) 080-5442002. Fax: (+39) 080-5442024.

## ACKNOWLEDGMENT

This work has been supported by PO Puglia FESR 2007–2013, Project 20.

## REFERENCES

- (1) Ulmann, A. *Thin Films: Self-Assembled Monolayers of Thiols*; Academic Press: San Diego, 1998.
- (2) Schreiber, F. *Prog. Surf. Sci.* **2000**, 65, 151.
- (3) Laibinis, P. E.; Whitesides, G. M.; Allara, D. L.; Tao, Y.-T.; Parikh, A. N.; Nuzzo, R. G. *J. Am. Chem. Soc.* **1991**, 113, 7152.
- (4) Ulman, A. *An Introduction to Ultrathin Organic Films: from Langmuir-Blodgett to Self-Assembly*; Academic Press: Boston, 1991.
- (5) Ulman, A. *Chem. Rev.* **1996**, 96, 1533.
- (6) Poirier, G. E. *Chem. Rev.* **1997**, 97, 1117.
- (7) Poirier, G. E.; Fitts, W. P.; White, J. M. *Langmuir* **2001**, 17, 1176.
- (8) Ulman, A. *Acc. Chem. Res.* **2001**, 34, 855.
- (9) Gozlan, N.; Tisch, U.; Haick, H. *J. Phys. Chem. C* **2008**, 112, 12988.
- (10) Oliveira, R. L.; Zanchet, D.; Kiyohara, P. K.; Rossi, L. M. *Chem.—Eur. J.* **2011**, 17, 4626.
- (11) Wang, X.; Andrews, L. *Angew. Chem., Int. Ed.* **2003**, 42, S201.
- (12) Letardi, S.; Cleri, F. *J. Chem. Phys.* **2004**, 120, 10062.
- (13) Biebuyck, H. A.; Bain, C. D.; Whitesides, G. M. *Langmuir* **1994**, 10, 1825.
- (14) Gun, J.; Rizkov, D.; Lev, O.; Abouzar, M. H.; Poghosian, A.; Schöning, M. J. *Microchim. Acta* **2008**, 164, 4395.
- (15) Bus, E.; van Bokhoven, J. A. *Phys. Chem. Chem. Phys.* **2007**, 9, 2894.
- (16) Boronat, M.; Concepción, P.; Corma, A.; González, S.; Illas, F.; Serna, P. *J. Am. Chem. Soc.* **2007**, 129, 16230.
- (17) Hesse, E.; Creighton, J. A. *Langmuir* **1999**, 15, 3545.

- (18) Wang, M.-C.; Liao, J.-D.; Weng, C.-C.; Klauser, R.; Frey, S.; Zharnikov, M.; Grunze, M. *J. Phys. Chem. B* **2002**, *106*, 6220.
- (19) Bruno, G.; Babudri, F.; Operamolla, A.; Bianco, G. V.; Losurdo, M.; Giangregorio, M. M.; Omar, O. H.; Mavelli, F.; Farinola, G. M.; Capezzuto, P.; Naso, F. *Langmuir* **2010**, *26*, 8430.
- (20) Bruno, G.; Bianco, G. V.; Giangregorio, M. M.; Sacchetti, A.; Capezzuto, P.; Losurdo, M. *Appl. Phys. Lett.* **2010**, *96*, 043104.
- (21) Losurdo, M.; Giangregorio, M. M.; Bianco, G. V.; Suvorova, A. A.; Kong, C.; Rubanov, S.; Capezzuto, P.; Humlicek, J.; Bruno, G. *Phys. Rev. B* **2010**, *82*, 155451.
- (22) Bruno, G.; Losurdo, M.; Capezzuto, P. *Appl. Phys. Lett.* **1995**, *66*, 3573.
- (23) Evans, S. D.; Ulman, A. *Chem. Phys. Lett.* **1990**, *170*, 462.
- (24) Evans, S. D.; Urankar, E.; Ulman, A.; Ferris, N. *J. Am. Chem. Soc.* **1991**, *113*, 4121.
- (25) Lu, J.; Delamarche, E.; Eng, L.; Bennewitz, R.; Meyer, E.; Guntherodt, H. J. *Langmuir* **1999**, *15*, 8184.
- (26) Alloway, D. M.; Hofmann, M.; Smith, D. L.; Gruhn, N. E.; Graham, A. L.; Colorado, R.; Wysocki, V. H.; Lee, T. R.; Lee, P. A.; Armstrong, N. R. *J. Phys. Chem. B* **2003**, *107*, 11690.
- (27) De Boer, B.; Hadipour, A.; Mandoc, M. M.; Van Woudenberg, T.; Blom, P. W. M. *Adv. Mater.* **2005**, *17*, 621.
- (28) McNally, H.; Janes, D. B.; Kasibhatla, B.; Kubiak, C. P. *Superlattices Microstruct.* **2002**, *31*, 239.
- (29) Chen, W.; Huang, C.; Gao, X. Y.; Wang, L.; Zhen, C. G.; Qi, D.; Chen, S.; Zhang, H. L.; Loh, K. P.; Chen, Z. K.; Wee, A. T. S. *J. Phys. Chem. B* **2006**, *110*, 26075.
- (30) Losurdo, M.; Bergmair, M.; Bruno, G.; Cattelan, D.; Cobet, C.; de Martino, A.; Fleischer, K.; Dohcevic-Mitrovic, Z.; Esser, N.; Galliet, M.; Gajic, R.; Hemzal, D.; Hingerl, K.; Humlicek, J.; Ossikovski, R.; Popovic, Z. V.; Saxl, O. *J. Nanopart. Res.* **2009**, *11*, 1521.
- (31) Ashcroft, N. W.; Mermin, N. D. *Solid State Physics*; Saunders College: Philadelphia, 1976.
- (32) Mulvaney, P.; Perez-Juste, J.; Giersing, M.; Liz-Marzan, L. M.; Pecharroman, C. *Plasmonics* **2006**, *1*, 61.
- (33) Pietron, J. J.; Hicks, J. F.; Murray, R. W. *J. Am. Chem. Soc.* **1999**, *121*, 5565.
- (34) Schwerdtfeger, P.; Boyd, P. D. W.; Brienne, S.; Burrell, A. K. *Inorg. Chem.* **1992**, *31*, 3411.
- (35) Aspnes, D. E.; Kinsbron, E.; Bacon, D. D. *Phys. Rev. B* **1980**, *21*, 3290.
- (36) Bus, E.; Miller, J. T.; van Bokhoven, J. A. *J. Phys. Chem. B* **2005**, *109*, 14581.
- (37) Stobirski, L.; Nowakowski, R.; Duś, R. *Vacuum* **1997**, *48*, 203.
- (38) Bus, E.; van Bokhoven, J. A. *Phys. Chem. Chem. Phys.* **2007**, *9*, 2894.
- (39) Willets, K. A.; Van Duyne, R. P. *Annu. Rev. Phys. Chem.* **2007**, *58*, 267.
- (40) McFarland, A. D.; Van Duyne, R. P. *Nano Lett.* **2003**, *3*, 1057.
- (41) Zhang, P.; Sham, T. K. *Appl. Phys. Lett.* **2002**, *81*, 736.
- (42) Hakkinen, H.; Barnett, R.; Landman, U. *Phys. Rev. Lett.* **1999**, *82*, 3264.
- (43) Shi, J.; Hong, B.; Parikh, A. N.; Collins, R. W.; Allara, D. L. *Chem. Phys. Lett.* **1995**, *246*, 90.
- (44) Damos, F. S.; Luz, R. C. S.; Kubota, L. T. *Langmuir* **2005**, *21*, 602.
- (45) Peterlinz, K. A.; Georgiadis, R. *Langmuir* **1996**, *12*, 4731.
- (46) Porter, M. D.; Bright, T. B.; Allara, D. L.; Chidsey, C. E. D. *J. Am. Chem. Soc.* **1987**, *109*, 3559.
- (47) Kondo, T.; Yanagida, M.; Shimazu, K.; Uosaki, K. *Langmuir* **1998**, *14*, 5656.
- (48) Laibinis, P. E.; Whitesides, G. M.; Allara, D. L.; Tao, Y. T.; Parikh, A. N.; Nuzzo, R. G. *J. Am. Chem. Soc.* **1991**, *113*, 7152.
- (49) Bradford, D. C.; Hutter, E.; Fendler, J. H.; Roy, D. *J. Phys. Chem. B* **2005**, *109*, 20914.
- (50) Mar, W.; Klein, M. L. *Langmuir* **1994**, *10*, 188.
- (51) Born, M.; Wolf, E. *Principles of Optics*; Pergamon Press: New York, 1965.
- (52) Cuyper, P. A.; Corsel, J. W.; Janssen, M. P.; Kop, J. M. M.; Hermens, W. Th.; Hemker, H. C. *J. Biol. Chem.* **1983**, *258*, 2426.
- (53) Howell, S.; Kuila, D.; Kasibhatla, B.; Kubiak, C. P.; Janes, D.; Reifengerger, R. *Langmuir* **2002**, *18*, 5120.
- (54) Rousseau, R.; De Renzi, V.; Mazzarello, R.; Marchetto, D.; Biagi, R.; Scandolo, S.; Pennino, U. *J. Phys. Chem. B* **2006**, *110*, 10862.
- (55) Saito, N.; Hayashi, K.; Sugimura, H.; Takai, O.; Nakagiri, N. *Surf. Interface Anal.* **2002**, *34*, 601.
- (56) Raiber, K.; Terfort, A.; Benndorf, C.; Krings, N.; Strehblow, H. *Surf. Sci.* **2005**, *595*, 56.